Instabilities and pattern miniaturization in confined and free elastic-viscous bilayers

Dipankar Bandyopadhyay, Ashutosh Sharma,[a] and V. Shankar
Department of Chemical Engineering, Indian Institute of Technology, Kanpur 208016, India

(Received 28 January 2008; accepted 26 February 2008; published online 17 April 2008)

We present an analysis of the instabilities engendered by van der Waals forces in bilayer systems composed of a soft elastic film (<10 μm) and a thin (<100 nm) viscous liquid film. We consider two configurations of such systems: (a) *Confined* bilayers, where the bilayer is sandwiched between two rigid substrates, and (b) *free* bilayers, where the viscous film is sandwiched between a rigid substrate and the elastic film. Linear stability analysis shows that the time and length scales of the instabilities can be tuned over a very wide range by changing the film thickness and the material properties such as shear modulus, surface tension, and viscosity. In particular, very short wavelengths comparable to the film thickness can be obtained in bilayers, which is in contrast to the instability wavelengths in single viscous and elastic films. It is also shown that the instabilities at the interfaces of the free bilayers are initiated via an in-phase "bending" mode rather than out-of-phase "squeezing" mode. The amplitudes of deformations at both the elastic-air and elastic-viscous interfaces become more similar as the elastic film thickness decreases and its modulus increases. These findings may have potential applications in the self-organized patterning of soft materials.
 [DOI: 10.1063/1.2899024]

I. INTRODUCTION

Instabilities of thin (<100 nm) polymer films has attracted much attention[1–13] because of their presence in various products and processes ranging from coatings, adhesives, flotation, and biological membranes to a host of areas in nanotechnology. In addition to the technological motivation, thin liquid films also serve as model mesoscale systems for the study of several fundamental scientific issues such as intermolecular forces, self-organization, confinement and finite-size effects, mesoscale dewetting, multilayer adsorption, and phase transitions. Therefore, much theoretical and experimental efforts have been devoted to understand the instability, dynamics, and final morphologies of thin films by various intermolecular forces, most notably the long-range van der Waals force.[1–13]

Recent experiments[14–27] on the stability of thin polymer bilayers have shown richer varieties of instabilities and dewetting pathways that are of potential use in mesoscale patterning of polymers for optoelectronic devices, microelectromechanical systems, and sensor applications. Experiments[22–27] show that when a solid film is bonded to a thick compliant substrate, which in turn bonded to a rigid substrate, the interfaces wrinkle into patterns such as labyrinths, stripes, and herringbones. Polymer bilayers are also a simple hydrodynamic model for the adhesion of a biological membrane[28,29] to a solid in the presence of a surrounding liquid.

From the fundamental standpoint, the instabilities in a thin bilayer have complex and interesting physics because it involves the dynamics of two coupled deformable interfaces. The presence of multiple and confined deformable interfaces in these bilayers can lead to two distinct initial modes[30,31] of deformations—in-phase *bending* and out-of-phase *squeezing*. Several recent studies have uncovered the different aspects of the long-wave instabilities in thin viscous bilayers[32–41] engendered by intermolecular forces. There are also several theoretical studies of periodic wrinkles[24–27,42–51] at the interfaces of the prestressed layered composites. However, the focus of all these studies is restricted to the larger thickness of the substrate-bonded films (>100 nm) where the intermolecular interactions are subdominant.

Recently, Martin[52] *et al.* have shown that the instabilities in the ultrathin substrate-bonded viscous films resting under a thick rubber layer are engendered by the van der Waals forces. Hosoi and Mahadevan[53] have presented a long-wave nonlinear analysis of a thin viscous layer with an elastic surface to explore the different motions, for example, peeling, healing, levitating, and bursting of a thin elastic sheet under the influence of the van der Waals forces present only in the viscous film. Kumar *et al.* have presented detailed long-wave linear[54] and nonlinear[55] analyses on the van der Waals force induced instabilities of a viscous film (a) resting on a substrate-bonded viscoelastic film and (b) sandwiched between a viscoelastic film and a solid substrate.

In this study, we discuss two different types of composite bilayers, as shown in Fig. 1. Figure 1(a) shows a confined bilayer where a substrate-bonded elastic film interacts with a rigid contactor in a purely viscous medium. This configuration is relevant for the understanding of contact instabilities in adhesion—a problem which has been studied when adhesion occurs in air.[56–66] In the present system, the adhesion occurs in a viscous liquid, which may influence the length and time scales of instability in soft adhesion. Previous

[a]Author to whom correspondence should be addressed. Electronic mail: ashutos@iitk.ac.in.

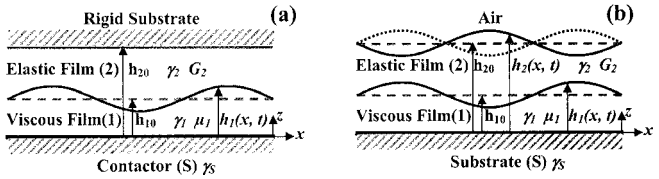

FIG. 1. Schematic diagrams of (a) *confined bilayer*—a substrate-bonded elastic film interacting with a contactor in a viscous medium and (b) *free bilayer*—an elastic film is resting on a viscous film, which in turn resting on a rigid substrate. The dotted line and the solid line at the elastic-air interface show *bending* and *squeezing* mode of deformations, respectively, with respect to the solid line at the elastic-viscous interface. In both diagrams, the mean thickness and the local thickness of the viscous layer are h_{10} and $h_1(x,t)$, respectively. The mean and local composite thicknesses are h_{20} and $h_2(x,t)$, respectively. γ_1, γ_2, and γ_s are the surface tensions of lower layer, upper layer, and the substrate respectively, G_2 is the shear modulus of the elastic film and μ_1 is the viscosity of the viscous film.

theoretical and experimental studies[56–66] revealed that the contact instability at the surface of an elastic film under the influence of an approaching contactor arises because of the interplay between the destabilizing intersurface adhesive interaction and the restoring elastic force of the film. The analyses[61,62,64] showed that when an elastic film is thick (>1.0 μm), the length scale of this instability is independent of all the material properties and linearly proportional to the elastic film thickness ($\lambda=nH$, where $n\sim3$). However, the proportionality factor n increases for the submicron thinner[64] films (<1.0 μm) because of the increasing influence of the surface tension force. The length scale of instability also increases compared to the case when the surface tension effects are ignored.[64] In this study, we show that the presence of the intercalated viscous film in the layered system [Fig. 1(a)] reduces the stabilizing effect of the surface tension force at the elastic-viscous interface and the length scale of instability can, thus, be reduced considerably for the systems with thinner elastic films. In addition, we propose a strategy for the miniaturization of the instability patterns using a bilayer. This can be achieved by initiating the instability from a configuration where the destabilizing forces are already much stronger than the stabilizing forces from the beginning. The length scale of instability in such systems is a function of the intermolecular interaction and the material properties of the films. Our analysis shows that the length scale significantly reduces when the intermolecular forces are strong and restoring elastic and capillary forces are weaker, which opens up the possibility of further miniaturization of the self-organized patterns exploiting contact instabilities in these layered systems.

Figure 1(b) shows the schematic diagram of a free bilayer where an elastic film floats on a substrate-bonded thin viscous (Newtonian) layer. In this study, we consider the most general analysis of a viscous-elastic bilayer where both films may be thin and the instabilities are not restricted to the long waves. In particular, our analysis emphasizes the following aspects. (A) While the previous studies[25,26,52–55] incorporated van der Waals interactions only within the viscous film, we consider intermolecular interactions in both layers to study the cases where both the films are thin (<100 nm) and the dynamics of the twin interfaces is strongly coupled. (B) We also extend the long-wave analysis of Martin[52] *et al.*, Hosoi and Mahadevan,[53] and Kumar and co-workers[54,55] to a generalized formulation of the instability that includes not just the long waves but also the short waves. Indeed, we show that the instability in many cases has a short wavelength comparable to the film thickness. (C) In addition to the most studied case of a *free bilayer*—an elastic film on a viscous film which, in turn, rests on a rigid substrate, we also consider the case of a *confined bilayer* where an elastic film bonded to a rigid substrate interacts with another rigid surface in a viscous medium. This geometry is a model of adhesion of a soft elastic film to another surface in a liquid medium.

In what follows, we focus on the instabilities that are engendered by the van der Waals forces in the two different elastic-viscous composite bilayers shown in Fig. 1. Starting with the equations of motion for the elastic and viscous layers, we carry out a linear stability analysis (LSA) and demonstrate the effect of the intermolecular interactions, the shear modulus of the elastic film, and the thicknesses of the films on the time and the length scale of instability.

II. PROBLEM FORMULATION

In this section, we first discuss the formulation for the free bilayer. The formulation for the confined bilayer is obtained by changing the boundary conditions at the elastic-air interface. In this study, we assume that the upper and the lower layers to be incompressible elastic solid and Newtonian incompressible liquid, respectively.

The coordinates parallel and normal to the substrate surface are denoted by x and z, respectively, and t represents time. We follow the convention where the subscript and superscript $i=1$ denote viscous layer and $i=2$ denotes elastic layer, s denotes the rigid substrate, and superscripts x and z denote variables corresponding to the respective coordinates. Thus, for the layer i, $u_x^{(i)}$ and $u_z^{(i)}$ are the x and z components of displacement, respectively, $v_x^{(i)}$ and $v_z^{(i)}$ are the x and z components of velocity, respectively, p_i is the pressure, and $P_i(=p_i-\pi_i)$ is the total (nonbody force) pressure. Here, π_i represents the disjoining pressures arising from the excess body force because of the intermolecular interactions (van der Waals forces) at the elastic-viscous ($i=1$) and elastic-air ($i=2$) interfaces, respectively. The viscosity of the liquid layer and the shear modulus of the elastic layer are denoted by μ_1 and G_2, respectively. The surface tension of the ith layer is γ_i, and γ_s is the surface energy of the rigid substrate. The base state thicknesses of the viscous, elastic, and composite layers are denoted by h_{10}, h_{30}, and h_{20}, respectively. The local composite and viscous layer thicknesses are represented by h_2 and h_1, respectively. Thus, $h_3=h_2-h_1$ is the elastic film thickness.

A. Governing equations

Since the dimensions are small, inertia is neglected for the liquid film. In the absence of inertia, the following two-dimensional equations of motion and the continuity equation describe the dynamics of the viscous layer:

$$-\frac{\partial P_1}{\partial x}+\mu_1\left(\frac{\partial^2 v_x^{(1)}}{\partial x^2}+\frac{\partial^2 v_x^{(1)}}{\partial z^2}\right)=0, \tag{1}$$

$$-\frac{\partial P_1}{\partial z}+\mu_1\left(\frac{\partial^2 v_z^{(1)}}{\partial x^2}+\frac{\partial^2 v_z^{(1)}}{\partial z^2}\right)=0, \tag{2}$$

$$\frac{\partial v_x^{(1)}}{\partial x}+\frac{\partial v_z^{(1)}}{\partial z}=0. \tag{3}$$

The equation of motion[67] without the body force and inertia for the elastic solid is $\nabla\cdot\sigma=0$, where $\sigma=K_2\nabla\cdot uI+G_2[(\nabla u+\nabla u^T)-(1/3)\nabla\cdot uI]$. Here, K_2 is the bulk modulus, I denotes identity matrix, and superscript T denotes transpose. For an incompressible solid film ($K_2\to\infty$ and $\nabla\cdot u=0$), the stress tensor reduces to the form $\sigma=-P_2I+G_2(\nabla u+\nabla u^T)$, where the product $K_2\nabla\cdot u$ is replaced by a mechanical-pressure-like variable $-P_2$ in the elastic solid,[67] and the momentum equation is supplemented by an explicit incompressibility condition $\nabla\cdot u=0$. Therefore, the following two-dimensional equations of motion and the condition for incompressibility describe the deformation in the elastic film:

$$-\frac{\partial P_2}{\partial x}+G_2\left(\frac{\partial^2 u_x^{(2)}}{\partial x^2}+\frac{\partial^2 u_x^{(2)}}{\partial z^2}\right)=0, \tag{4}$$

$$-\frac{\partial P_2}{\partial z}+G_2\left(\frac{\partial^2 u_z^{(2)}}{\partial x^2}+\frac{\partial^2 u_z^{(2)}}{\partial z^2}\right)=0, \tag{5}$$

$$\frac{\partial u_x^{(2)}}{\partial x}+\frac{\partial u_z^{(2)}}{\partial z}=0. \tag{6}$$

The equations of motion used for the elastic film in this study are, thus, similar to the formalism used in the related works of Sarkar *et al.*[61,62] and Kumar and co-workers.[54,55]

B. Boundary conditions

We assume that the viscous film is perfectly bonded to the rigid substrate and, therefore, at $z=0$, the no slip and the impermeability boundary conditions are applied,

$$v_x^{(1)}=v_z^{(1)}=0. \tag{7}$$

At $z=h_1$, the continuity of x and z components of velocities, normal stress balance, shear stress balance, and the kinematic condition are applied as the boundary conditions,

$$v_x^{(1)}=\frac{\partial u_x^{(2)}}{\partial t}, \tag{8}$$

$$v_z^{(1)}=\frac{\partial u_z^{(2)}}{\partial t}, \tag{9}$$

$$P_1-P_2-2\mu_1\frac{\partial v_z^{(1)}}{\partial z}+2G_2\frac{\partial u_z^{(2)}}{\partial z}+\pi_1-\pi_2+\gamma_{21}\frac{\partial^2 h_1}{\partial x^2}=0, \tag{10}$$

$$\mu_1\left(\frac{\partial v_x^{(1)}}{\partial z}+\frac{\partial v_z^{(1)}}{\partial x}\right)=G_2\left(\frac{\partial u_x^{(2)}}{\partial z}+\frac{\partial u_z^{(1)}}{\partial x}\right), \tag{11}$$

$$\frac{\partial h_1}{\partial t}+v_x^{(1)}|_{h_1}\frac{\partial h_1}{\partial x}=v_z^{(1)}|_{h_1}, \tag{12}$$

where $a|_{h_i}$ implies any variable a evaluated at thickness h_1 and γ_{21} is the interfacial tension at the elastic-viscous interface obtained from the relation, $(\sqrt{\gamma_2}-\sqrt{\gamma_1})^2$.[68,69]

At $z=h_2$, the normal and shear stress balances and the kinematic condition are applied as boundary conditions,

$$P_2-2G_2\frac{\partial u_z^{(2)}}{\partial z}+\pi_2+\gamma_2\frac{\partial^2 h_2}{\partial x^2}=0, \tag{13}$$

$$G_2\left(\frac{\partial u_x^{(2)}}{\partial z}+\frac{\partial u_z^{(2)}}{\partial x}\right)=0, \tag{14}$$

$$\frac{\partial h_2}{\partial t}+\left.\frac{\partial u_x^{(2)}}{\partial t}\right|_{h_2}\frac{\partial h_2}{\partial x}=\left.\frac{\partial u_z^{(2)}}{\partial t}\right|_{h_2}. \tag{15}$$

Here, π_1 and π_2 are the van der Waals disjoining pressures (negative of conjoining pressures) at the two interfaces, given by[1–6,31]

$$\pi_1=-\frac{A_1}{6\pi h_1^3}-\frac{A_2}{6\pi h_2^3}, \tag{16}$$

$$\pi_2=-\frac{A_3}{6\pi h_3^3}-\frac{A_2}{6\pi h_2^3}. \tag{17}$$

Equations (16) and (17) are derived from the simplest potential that can describe a bilayer system,

$$\Delta G=-\frac{A_1}{12\pi h_1^2}-\frac{A_2}{12\pi h_2^2}-\frac{A_3}{12\pi h_3^2}, \tag{18}$$

where $\pi_1=\partial(-\Delta G)/\partial h_1$ and $\pi_2=\partial(-\Delta G)/\partial h_3$. Potentials in Eqs. (16)–(18) are written in terms of effective Hamaker constants (A_i) which, in turn, are derived from the binary Hamaker constants (A_{ij}),

$$A_1=A_{11}+A_{s2}-A_{s1}-A_{12},$$

$$A_2=A_{s2}-A_{12},$$

$$A_3=A_{22}-A_{12}.$$

The binary Hamaker constants (A_{ij}) are of the materials denoted by their subscripts (s, 1, and 2). The indices of effective Hamaker (A_i) constants, however, do not follow this convention. A positive effective Hamaker constant for a single layer implies an attractive force leading to spinodal instability and its negative value corresponds to thermodynamic stability.[1–10]

III. LINEAR STABILITY

A. General dispersion relation

In this section, we first carry out the LSA and derive the dispersion relation for the free bilayer. The following two assumptions hold good under the limit of linear theory: (i) The kinematics of deformation of the elastic film is treated

using a small-deformation formulation and (ii) the disjoining pressures are expanded in Taylor series about the base state and terms up to first order are retained,

$$\pi_1(h_{10}+\varepsilon_1,h_{20}+\varepsilon_2) = \pi_1(h_{10},h_{20}) + \left[\left(\frac{\partial \pi_1}{\partial h_1}\right)\varepsilon_1 + \left(\frac{\partial \pi_1}{\partial h_2}\right)\varepsilon_2\right],$$

$$\pi_2(h_{10}+\varepsilon_1,h_{20}+\varepsilon_2) = \pi_2(h_{10},h_{20}) + \left[\left(\frac{\partial \pi_2}{\partial h_1}\right)\varepsilon_1 + \left(\frac{\partial \pi_2}{\partial h_2}\right)\varepsilon_2\right].$$

Here, ε_1 and ε_2 are, respectively, the infinitesimal perturbations at the elastic-viscous and elastic-air interfaces. Equations (1)–(6) are linearized using normal modes $v_x^{(1)} = \tilde{v}_x^{(1)} e^{\omega t+ikx}$, $v_z^{(1)} = \tilde{v}_z^{(1)} e^{\omega t+ikx}$, $u_x^{(2)} = \tilde{u}_x^{(2)} e^{\omega t+ikx}$, $u_z^{(2)} = \tilde{u}_z^{(2)} e^{\omega t+ikx}$, $P_j = \tilde{P}_j e^{\omega t+ikx}$, and $h_j = h_{j0} + \varepsilon_i e^{\omega t+ikx}$, where $j=1$ and 2. The variables $\tilde{v}_x^{(1)}$, $\tilde{v}_z^{(1)}$, $\tilde{u}_x^{(2)}$, $\tilde{u}_z^{(2)}$, $\tilde{P}_j$, and ε_j are functions of z only, ω and k represent the linear growth coefficient and the wave number of disturbance, respectively, and $i=\sqrt{-1}$,

$$-ik\tilde{P}_1 + \mu_1\left(-k^2\tilde{v}_x^{(1)} + \frac{\partial^2 \tilde{v}_x^{(1)}}{\partial z^2}\right) = 0, \tag{19}$$

$$-\frac{\partial \tilde{P}_1}{\partial z} + \mu_1\left(-k^2\tilde{v}_z^{(1)} + \frac{\partial^2 \tilde{v}_z^{(1)}}{\partial z^2}\right) = 0, \tag{20}$$

$$ik\tilde{v}_x^{(1)} + \frac{\partial \tilde{v}_z^{(1)}}{\partial z} = 0, \tag{21}$$

$$-ik\tilde{P}_2 + G_2\left(-k^2\tilde{u}_x^{(2)} + \frac{\partial^2 \tilde{u}_x^{(2)}}{\partial z^2}\right) = 0, \tag{22}$$

$$-\frac{\partial \tilde{P}_2}{\partial z} + G_2\left(-k^2\tilde{u}_z^{(2)} + \frac{\partial^2 \tilde{u}_z^{(2)}}{\partial z^2}\right) = 0, \tag{23}$$

$$ik\tilde{u}_x^{(2)} + \frac{\partial \tilde{u}_z^{(2)}}{\partial z} = 0. \tag{24}$$

Eliminating $\tilde{P}_1$ and $\tilde{P}_2$ from the linearized governing equations [(19)–(24)] results in the following biharmonic equations for the variables $\tilde{v}_z^{(1)}$ and $\tilde{u}_z^{(2)}$:

$$\frac{d^4\tilde{v}_z^{(1)}}{dz^4} - 2k^2\frac{d^2\tilde{v}_z^{(1)}}{dz^2} + k^4\tilde{v}_z^{(1)} = 0, \tag{25}$$

$$\frac{d^4\tilde{u}_z^{(2)}}{dz^4} - 2k^2\frac{d^2\tilde{u}_z^{(2)}}{dz^2} + k^4\tilde{u}_z^{(2)} = 0. \tag{26}$$

The general solutions of Eqs. (25) and (26) are as follows:

$$\tilde{v}_z^{(1)} = (A_1 + A_2 z)\exp(kz) + (A_3 + A_4 z)\exp(-kz), \tag{27}$$

$$\tilde{u}_z^{(2)} = (B_1 + B_2 z)\exp(kz) + (B_3 + B_4 z)\exp(-kz), \tag{28}$$

where the coefficients A_i and B_i $(i=1-4)$ are constants. The boundary conditions [(7)–(15)] are linearized in the following manner: At $z=0$,

$$\tilde{v}_x^{(1)} = \tilde{v}_z^{(1)} = 0. \tag{29}$$

$$\tilde{v}_x^{(1)} = \omega\tilde{u}_x^{(2)}, \quad \tilde{v}_z^{(1)} = \omega\tilde{u}_z^{(2)}, \tag{30}$$

$$\tilde{P}_1 - \tilde{P}_2 - 2\mu_1\frac{\partial \tilde{v}_z^{(1)}}{\partial z} + 2G_2\frac{\partial \tilde{u}_z^{(2)}}{\partial z} + \left|\left(-k^2\gamma_{21} + \frac{\partial \pi_1}{\partial h_1} - \frac{\partial \pi_2}{\partial h_1}\right)\frac{\tilde{v}_z^{(1)}}{\omega}\right|_{h_{10},h_{20}} + \left|\left(\frac{\partial \pi_1}{\partial h_2} - \frac{\partial \pi_2}{\partial h_2}\right)\tilde{u}_z^{(2)}\right|_{h_{10},h_{20}} = 0, \tag{31}$$

$$\mu_1\left(\frac{\partial \tilde{v}_x^{(1)}}{\partial z} + ik\tilde{v}_z^{(1)}\right) - G_2\left(\frac{\partial \tilde{u}_x^{(2)}}{\partial z} + ik\tilde{u}_z^{(2)}\right) = 0, \tag{32}$$

$$\varepsilon_1 = \left.\frac{\tilde{v}_z^{(1)}}{\omega}\right|_{h_1}. \tag{33}$$

At $z=h_2$,

$$\tilde{P}_2 - 2G_2\frac{\partial \tilde{u}_z^{(2)}}{\partial z} + \left|\left(-k^2\gamma_2 + \frac{\partial \pi_2}{\partial h_2}\right)\tilde{u}_z^{(2)}\right|_{h_{10},h_{20}} + \left(\frac{\partial \pi_2}{\partial h_1}\right)\frac{\tilde{v}_z^{(1)}}{\omega}\Bigg|_{h_{10},h_{20}} = 0, \tag{34}$$

$$\left(\frac{\partial \tilde{u}_x^{(2)}}{\partial z} + ik\tilde{u}_z^{(2)}\right) = 0, \tag{35}$$

$$\varepsilon_2 = \tilde{u}_z^{(2)}|_{h_2}. \tag{36}$$

The general solutions for $\tilde{v}_z^{(1)}$ and $\tilde{u}_z^{(2)}$ [Eqs. (27) and (28)] are used to obtain the expressions for all the remaining unknown linearized variables $\tilde{v}_x^{(1)}$, $\tilde{u}_x^{(2)}$, $\tilde{P}_1$, and $\tilde{P}_2$. Replacing the expressions of these variables ($\tilde{v}_z^{(1)}$, $\tilde{u}_z^{(2)}$, $\tilde{v}_x^{(1)}$, $\tilde{u}_x^{(2)}$, $\tilde{P}_1$, and $\tilde{P}_2$) in the boundary conditions [(29)–(36)] lead to a set of eight homogeneous linear algebraic equations involving eight unknown constants A_i and B_i $(i=1-4)$. By equating the determinant of the coefficient matrix of these linear equations to 0, we get the general dispersion relation for the free bilayers shown in the Appendix [Eq. (A1)]. The operations in this derivation were also verified with the help of the symbolic package MATHEMATICA™. The solution of the dispersion relation leads to an analytical expression for the growth coefficient of the instability as a function of the wave number $[\omega=f(k)]$. The necessary condition for the instability is $\mathrm{Re}\{\omega\}>0$. The dominant growth coefficient (ω_m) and the corresponding wavelength (λ_m) of instability are obtained by finding the global maxima of ω and the corresponding wavelength, respectively, from the dispersion relation.

The dispersion relation for the confined bilayer [Fig. 1(a)] is also shown in the Appendix [Eq. (A2)]. This is obtained by replacing the normal and tangential stress balances [Eqs. (34) and (35)] at the elastic-air interface $(z=h_2)$ by the rigid and impermeable boundary condition, $\tilde{u}_x^{(2)} = \tilde{u}_z^{(2)} = 0$, and then carrying out the similar operations as it was done for the free bilayer.

As a limiting case, we have verified that the general dispersion relation [Eq. (A1) in the Appendix] reduces to the dispersion relation of a single dewetting liquid film resting on a rigid substrate, when $h_3 \to 0$.[10] In addition, the dispersion relation for the confined bilayer [Eq. (A2) in the Appendix] reduces to the dispersion relation of the soft elastic film rigidly bonded to the substrate and interacting with a contactor in air in the limit of $\mu_1 \to 0$.[64]

B. Relative deformations at the interfaces of the free bilayers

The modes (squeezing or bending) and the subsequent relative interfacial deformations at the interfaces for the free bilayer [Fig. 1(b)] can also be predicted from the LSA. Initially, we assume an infinitesimal deformation $\varepsilon_2 = f(z)$ at the elastic-air interface in the z direction. It can be expressed in terms of the linear displacement at $z=h_2$ in the following manner:

$$\tilde{u}_z^{(2)} = \varepsilon_2. \tag{37}$$

In response to this, the linearized x and z components of infinitesimal displacement at the elastic-viscous interface ($z=h_1$) are assumed as $\varepsilon_3 = f(z)$ and $\varepsilon_1 = f(z)$, respectively, and can be expressed in the following forms:

$$\tilde{u}_z^{(2)} = \varepsilon_1, \quad \tilde{u}_x^{(2)} = \varepsilon_3. \tag{38}$$

By using the boundary condition shown in Eq. (30), the linearized z and x components of the velocities at $z=h_1$ for the viscous film can be written as follows:

$$\tilde{v}_x^{(1)} = \varepsilon_3 \omega, \quad \tilde{v}_z^{(1)} = \varepsilon_1 \omega. \tag{39}$$

The general solutions for $\tilde{v}_z^{(1)}$ and $\tilde{u}_z^{(2)}$ are already shown in the Eqs. (27) and (28). The coefficients A_i and B_i ($i=1-4$) of those linear equations are evaluated using the following boundary conditions: (i) At $z=0$; the no slip and the impermeability [Eq. (29)], (ii) at $z=h_1$ and h_2, the five boundary conditions mentioned in Eqs. (37)–(39), and (iii) at $z=h_2$, tangential stress balance [Eq. (35)]. The expressions for A_i and B_i ($i=1-4$), thus, obtained are $f(\varepsilon_1, \varepsilon_2, \varepsilon_3, G_2, \mu_1, h_{10}, h_{30}, \phi_1, \phi_2, \phi_4, \omega, k)$. For a particular free bilayer G_2, μ_1, h_{10}, h_{30}, ϕ_1, ϕ_2, and ϕ_4 are known. The expressions for maximum linear growth coefficient (ω_m) and the corresponding wave number (k_m) can be obtained from the general dispersion relation [Eq. (A1) in the Appendix] and is replaced for ω and k in the expressions for A_i and B_i ($i=1-4$), respectively. Therefore, the expressions for the coefficients A_i and B_i ($i=1-4$) now become $f(\varepsilon_1, \varepsilon_2, \varepsilon_3)$ only. Thereafter, the following three unused boundary conditions are expressed as $f(\varepsilon_1, \varepsilon_2, \varepsilon_3)$ using the expressions for A_i and B_i ($i=1-4$): (i) Normal stress balance at the elastic-viscous interface [Eq. (31)], (ii) tangential stress balance at the elastic-viscous interface [Eq. (32)], and (iii) normal stress balance at the elastic-air interface [Eq. (34)]. We cannot obtain explicit expressions for ε_1, ε_2, and ε_3 from the above three boundary conditions because the resulting equations are homogeneous in nature. Therefore, any two of the above-mentioned three boundary conditions can be used to evaluate the expressions for $\varepsilon_2/\varepsilon_3$ and $\varepsilon_1/\varepsilon_3$. The ratios $\varepsilon_2/\varepsilon_3$ and $\varepsilon_1/\varepsilon_3$ represent the relative amplitudes of deformation $\varepsilon_r (=\varepsilon_2/\varepsilon_1)$ at the interfaces. The expression of ε_r is very cumbersome and is, thus, not displayed in the text. Only the numerical computations are shown.

The sign and the magnitude of ε_r, evaluated using ω_m and k_m, yield information about the fastest deforming mode and the resulting relative amplitudes at the interfaces, respectively. A bending mode of deformation results if $\varepsilon_r > 0$ and a squeezing mode ensues if $\varepsilon_r < 0$. Further, the upper interface deforms more when $|\varepsilon_r| > 1$, the lower interface deforms more when $|\varepsilon_r| < 1$, and the deformations are same at the interfaces when $|\varepsilon_r| = 1$.

IV. RESULTS AND DISCUSSIONS

In what follows, we first discuss the LSA results obtained for the confined bilayer [Fig. 1(a)] followed by the results for the free bilayer [Fig. 1(b)].

A. Confined bilayers: Instabilities of deforming elastic-viscous interface

In a confined bilayer, the interaction and adhesion of the soft elastic film with the rigid contactor take place in a viscous medium under the influence of an attractive intersurface force. The capillary forces at the elastic-viscous interface and the restoring elastic forces in the elastic film impede the onset of instability. Elastic films with higher shear modulus (G_2) and lower thickness (h_{30}) are less susceptible to deformation and are, hence, more stable. We define the ratio G_2/h_{30} as the measure of the compliancy of the elastic film. The instabilities in these layered systems can be initiated in two different ways, which we term as "mode I" and "mode II," as discussed below.

1. Mode I: Definition and characteristics of the instabilities

To initiate the instabilities in this mode, a rigid contactor is gradually brought closer toward the free surface of the substrate-bonded elastic film, which is immersed in a pool of viscous liquid. At a threshold separation distance between the contactor and the elastic-viscous interface, where the intersurface attractive force marginally overcomes the restoring elastic and surface tension forces, the surface roughening at the elastic-viscous interface takes place. The following condition for the balance of the forces can be obtained by imposing the neutral stability condition ($\omega=0$) to the dispersion relation [Eq. (A2) in the Appendix]:

$$\phi = \frac{A_1}{2\pi h_{10}^4} = \gamma_{21} k^2 - \frac{2kG_2[(1+e^{2kh_{30}})^2 + 4e^{2kh_{30}}k^2h_{30}^2]}{1 - e^{4kh_{30}} + 4e^{2kh_{30}}kh_{30}}. \tag{40}$$

Interestingly, the expression shown in Eq. (40) exactly matches with the dispersion relation obtained for a substrate-bonded soft elastic film interacting with an approaching contactor in air.[64] This indicates that the presence of the viscous liquid has no role in the condition for the initiation of the instability. This result can be anticipated on the physical ground because the viscosity being a transport property does

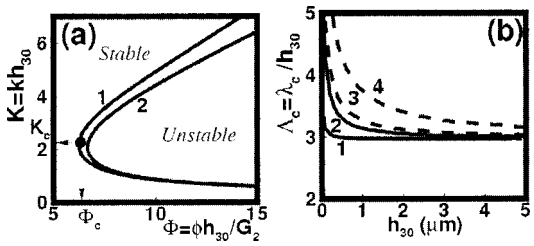

FIG. 2. Plot (a) shows the variation of Φ with K. The curves 1 and 2 correspond to $h_{30}=1.0$ and 0.15 μm. The other parameters in the plots are $\gamma_{12}=0.008$ N/m and $G_2=10^6$ Pa. Plot (b) shows the variation of λ_c/h_{30} with h_{30}. The broken lines correspond to $G_2=10^5$ Pa and the solid lines correspond to $G_2=10^5$ Pa. In curves 1 and 2, γ_{12} is kept at 0.005 and 0.05 N/m, respectively, and in curves 3 and 4, $\gamma_{12}=0.01$ and 0.03 N/m, respectively. In all plots, $h_{10}=5$ nm.

not affect the purely thermodynamic considerations at the neutral stability, where the instability growth is vanishingly small.

Equation (40) reduces to the following compact form using the nondimensional parameters $\Phi=\phi h_{30}/G_2$, $K=kh_{30}$, and $\bar{\gamma}=\gamma_{21}/G_2h_{30}$:

$$\Phi = \bar{\gamma}K^2 - \frac{2K[(1+e^{2K})^2+4K^2e^{2K}]}{1-e^{4K}+4Ke^{2K}}. \tag{41}$$

Figure 2(a) shows a bifurcation diagram [Φ vs K plots from Eq. (41)] in which the *bifurcation point* (corresponding to Φ_c and K_c) corresponds to the *critical condition* or the critical attractive force for the onset of instability. Under this condition, the destabilizing and stabilizing forces exactly balance each other and an infinitesimal increase in the destabilizing intermolecular force from this value, for example, by moving the contactor closer toward the elastic-viscous interface, creates surface inhomogeneities at the elastic-viscous interface with a lateral length scale of $\Lambda_c(=\lambda_c/h_{30})$ corresponding to the *critical* wave number $K_c(=2\pi/\Lambda_c)$. Figure 2(b) shows the variation of Λ_c with h_{30}. All the curves in Fig. 2(b) show that when the elastic film is relatively thick (high h_{30}), the wavelength scaling is $\Lambda_c\sim 3$. Further, it is independent of the shear modulus of the elastic film and the surface tension. However, for low h_{30}, increasing influence of the elastic-viscous interfacial tension (γ_{21}) shifts the length scale of instability to the longer wavelength regime.[64] In practice, the presence of viscous film reduces γ_{21} by an order of magnitude at elastic-viscous interface in the confined bilayer as compared to the systems where the viscous film is absent. Figure 2(b) shows that smaller γ_{21} at the elastic-viscous interface in a composite bilayer leads to smaller length scales at low h_{30} (curve 1 or 3) as compared to the system where γ_{21} is large (curve 2 or 4). For example, a layered system with a 100 nm elastic film (shear modulus of 10^5 Pa) and a 5 nm viscous film shows a length scale of $\sim 7h_{30}$ when the interfacial tension is 0.045 N/m. This length scale reduces to $\sim 4h_{30}$ when the interfacial tension is lowered to 0.005 N/m.

2. Mode II: Definition and characteristics of the instabilities

In this mode, we envisage an experiment where a thin polymer film below its glass transition temperature (T_g) is initially coated on a substrate-bonded soft elastic film and a contactor is placed on the polymer film. The polymer film thickness is considered to be in the regime where the bilayer is unstable. The lower thickness of the coated polymer film ensures that the intermolecular forces remain much stronger than the combined restoring forces arising from the elastic and surface tension forces in the initial configuration. Once the polymer layer is heated above the T_g, the thin polymer film melts and surface roughening at the elastic-viscous interface can take place. In this unstable system, the length scale of instability corresponds to the dominant wavelength (λ_m) associated with the maximum of the growth coefficient (ω_m).

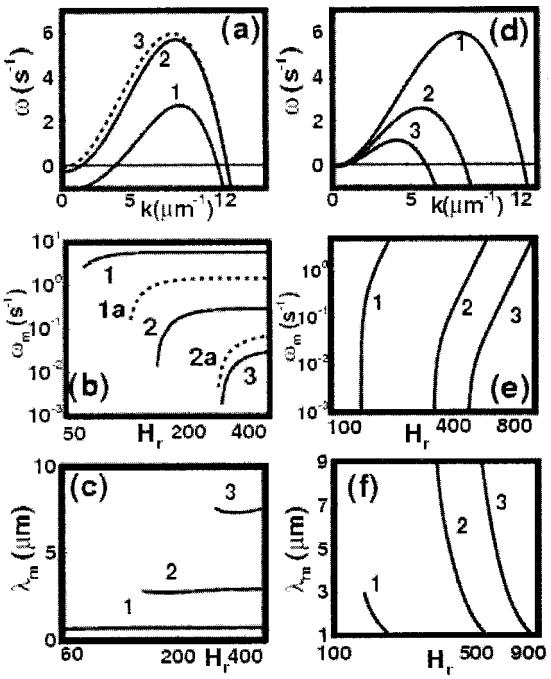

FIG. 3. Plots (a) and (d) show the variation of ω with k, plots (b) and (e) show the variation of ω_m with H_r, and plots (c) and (f) show the variation λ_m with H_r. In plot (a), curves 1–3 correspond to $h_{30}=0.3$, 0.5, and 0.9 μm, respectively, when $h_{10}=5.0$ nm. In plots (b) and (c), the curves 1–3 correspond to $h_{10}=5.0$, 7.0, and 9.0 nm, respectively, when $G_2=10^6$ Pa and the curves 1a and 2a correspond to $h_{10}=5.0$ and 7.0 nm, respectively, when $G_2=2.0\times 10^6$ Pa. In plot (d), curves 1–3 correspond to $h_{10}=5.0$, 5.5, and 6.0 nm, respectively, when $h_{30}=1.0$ μm. In plots (e) and (f), curves 1–3 correspond to $h_{30}=1.0$, 3.0, and 5.0 μm, respectively. In the plots, $\gamma_1=0.015$ N/m, $\gamma_2=0.045$, $A_1=10^{-19}$ J, $\mu_1=1.0$ Pa s, and $G_2=10^6$ Pa.

Figure 3 shows the LSA results for this system when the relative film thicknesses are varied. Bilayers with relatively thin elastic layer (low H_r) are more stable (lower ω_m) because the thinner elastic films are less compliant and, hence, less deformable [Figs. 3(a) and 3(b)]. With progressive increase in h_{30} (increasing H_r), the increase in compliance of the elastic films leads to the increase in ω_m [Fig. 3(b)]. The dimensionless number $d=G_2/\phi h_{30}=1/\Phi$ can quantify the effect of compliancy on the instability. For the curves shown in Fig. 3(b), d is high at smaller h_{30} and d reduces to ~ 0.03, when ω_m is independent of h_{30}. This indicates that for $d>0.03$, the compliancy of the elastic film plays a role and with increase in h_{30}, the system becomes more unstable (ω_m increases). However, when $d<0.03$, ω_m becomes constant and increased compliancy in the elastic film because of the

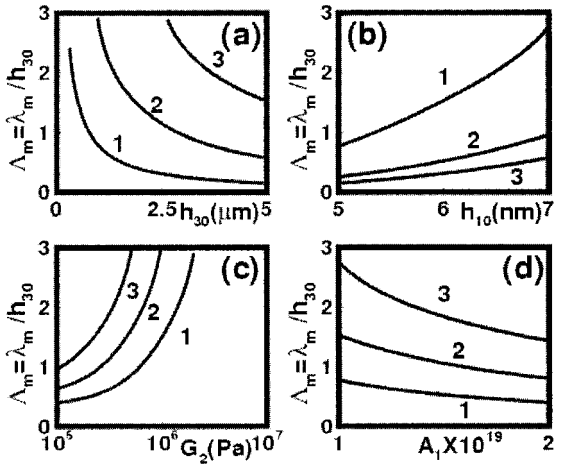

FIG. 4. Plots (a), (b), (c), and (d) show variations of λ_m/h_{30} with h_{30}, h_{10}, G_2, and A_1, respectively. In plot (a), curves 1–3 correspond to $h_{10}=5.0$, 7.0, and 8.0 nm, respectively, when $G_2=10^6$ and $A_1=10^{-19}$ J. In plot (b), curves 1–3 correspond to $h_{30}=1.0$, 3.0, and 5.0 μm, respectively, and $G_2=10^6$ and $A_1=10^{-19}$ J. Curves 1–3 in plot (c) and (d) correspond to $h_{10}=5.0$, 6.0, and 7.0 nm, respectively. In plot (c), $h_{30}=1.0$ μm and $A_1=10^{-19}$ J, and in plot (d), $h_{30}=1.0$ μm and $G_2=10^6$ Pa. In all the plots, $\gamma_1=0.015$ N/m, $\gamma_2=0.045$, and $\mu_1=1.0$ Pa s.

increase in h_{30} that plays no further role in destabilizing the system. Figure 3(c) shows that the dominant length scale of instability λ_m is almost independent of the change in h_{30}. Figures 3(d)–3(f) show that ω_m and λ_m changes very sharply with the change in h_{10}. Reduction in h_{10} increases the strength of the intermolecular interaction and makes the system more unstable which is reflected in the increases in ω_m [Fig. 3(e)] and reduction in λ_m [Fig. 3(f)]. In Fig. 4, the sensitivity of the normalized length scale ($\Lambda_m=\lambda_m/h_{30}$) of the instability on different parameters such as intermolecular force, G_2, h_{10}, and h_{30} is shown. This figure shows that Λ_m can be markedly reduced by (i) increasing h_{30} [Fig. 4(a)] and reduction in G_2 [Fig. 4(c)] and (ii) strengthening the intermolecular interaction by decreasing h_{10} [Fig. 4(b)] and increasing A_1 [Fig. 4(d)]. A thicker elastic film is more deformable because it is more compliant and the surface tension forces no longer acts as a stabilizing influence. In addition, elastic films with lower shear modulus have less elastic resistance toward deformation. Therefore, when the intermolecular forces are very strong, bilayers with thick elastic films and low shear modulus show a smaller length scale of instability. For example, a system with elastic film thickness of 1 μm and shear modulus of 10^6 Pa shows a length scale of $3h_{30}$ when the viscous film is 7 nm thin, whereas the wavelength decreases to $\sim h_{30}$ upon reduction of the viscous film thickness to 5 nm. It is interesting to recall here that the length scale of instability on a substrate-bonded elastic film deforming under the influence of a contactor[56–66] in air is independent of the interaction and material properties of the film and show $\Lambda_m\sim 3$. In contrast, Fig. 4 clearly shows that much smaller length scales can be achieved for confined bilayers by increasing the strength of the destabilizing forces and reducing the strength of the restoring forces. This opens up the possibility of miniaturization of patterns using confined bilayers, which is not possible in purely viscous or elastic single layers.

B. Free bilayers: Instabilities of elastic-air and elastic-viscous interfaces

The dispersion relation [Eq. (A1) in the Appendix] for the free bilayers can be reduced to the following necessary condition for instability in three steps: (i) By expanding it in a power series in k, (ii) retaining all lower order k terms, and (iii) applying the neutral stability condition ($\omega=0$),

$$4G_2\left[\left(-\gamma_{21}k^2+\frac{\partial\pi_1}{\partial h_1}-\frac{\partial\pi_2}{\partial h_1}\right)+\left(\frac{\partial\pi_1}{\partial h_2}-\frac{\partial\pi_2}{\partial h_2}\right)+\frac{\partial\pi_2}{\partial h_1}+\left(-\gamma_2k^2+\frac{\partial\pi_2}{\partial h_2}\right)\right]+h_3\left[\left(\frac{\partial\pi_1}{\partial h_2}-\frac{\partial\pi_2}{\partial h_2}\right)\frac{\partial\pi_2}{\partial h_1}-\left(-\gamma_{21}k^2+\frac{\partial\pi_1}{\partial h_1}-\frac{\partial\pi_2}{\partial h_1}\right)\left(-\gamma_2k^2+\frac{\partial\pi_2}{\partial h_2}\right)\right]>0 \tag{42}$$

Equation (42) shows that the capillary forces at the interfaces impede the onset of instability. Neglecting the capillary forces in Eq. (42) by setting $k=0$ and then substituting for the intermolecular forces from Eqs. (16) and (17) leads to the following simplified form of the necessary condition for instability:

$$\left(\frac{4G_2}{h_{30}}-\frac{A_3}{2\pi h_{30}^4}\right)\left(-\frac{A_1}{h_{10}^4}-\frac{A_2}{h_{20}^4}\right)+\left(\frac{A_1A_2}{12\pi h_{10}^4h_{20}^4}\right)<0. \tag{43}$$

Equation (43) suggests that (i) elastic forces in the solid layer resist the onset of instability, (ii) the attractive (A_1, A_2, and $A_3>0$) intermolecular forces has destabilizing influence, and (iii) repulsive (A_1, A_2, and $A_3<0$) intermolecular forces stabilize the system. For ease of analysis in the following sections, the total free energy of bilayers [Eq. (18)] is split in the following manner: $\Delta g_1=-A_1/12\pi h_1^2$, $\Delta g_2=-A_2/12\pi h_2^2$, $\Delta g_3=-A_3/12\pi h_3^2$, and $\Delta G=\Sigma_{i=1}^3\Delta g_i$. Negative and positive free energy indicate the presence of an attractive and repulsive intermolecular forces, respectively. The forces are stronger when the film thicknesses are small. In general, the larger denominator (h_2 is always $>h_1$ and h_3) in the expression of Δg_2 always makes the corresponding force less significant compared to the forces because of Δg_1 and Δg_3.

In practice, the free bilayers can be prepared by coating a very thin polymer film (below its T_g) on a rigid substrate and then coating an elastic film on the polymer film. Thereafter, when this layered system is heated above the T_g of the polymer film, the polymer film melts and instabilities at the elastic-viscous and elastic-air interfaces can be observed. Unlike the confined bilayer where $\omega<0$ in the limit of $k\to 0$ [Fig. 3(a)], this instability persists even in the long-wave regime ($k\to 0$) because of deformable nature of the elastic-air interface. However, there exists a dominant mode associated with ω_m at finite $k(=k_m)$ and the instability grows following the length scale λ_m corresponding to ω_m.

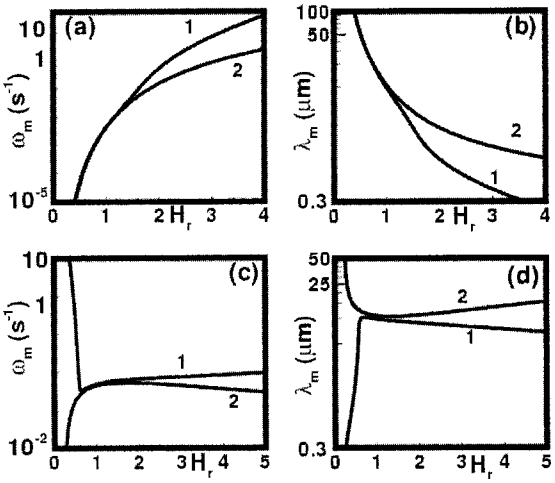

FIG. 5. LSA results for case 1 free bilayer. Plots (a) and (b) show the variations of ω_m and λ_m with $H_r(=h_{30}/h_{10})$ when $h_{30}=20$ nm. Plots (c) and (d) show the variations of ω_m and λ_m with $H_r(=h_{30}/h_{10})$ when $h_{10}=20$ nm. Curves 1 and 2 in all the plots correspond to $G_2=10^3$ and 10^9 Pa, respectively. In all the plots $A_3=3.58\times10^{-20}$ J, $A_2=1.05\times10^{-19}$ J, $A_1=4.47\times10^{-20}$ J, and $\mu_1=1.0$ Pa s.

In what follows, free bilayers are classified based on the nature of the destabilizing intermolecular forces present. We then discuss the roles of shear modulus of the elastic film, interfacial tensions, and film thicknesses on (i) the time and length scales of instability and (ii) the modes (squeezing or bending) of deformations and its amplitudes. We show that the length scale of instability for free bilayers is a function of the intermolecular interaction and material properties. In addition, we present a comparison between the length scales of instabilities that can be achieved from this configuration and the previously studied systems.[56–66]

1. Case 1: Unstable elastic and viscous films ($A_1>0$ and $A_3>0$)

In this case, the intermolecular forces because of Δg_3 ($A_3>0$) and Δg_1 ($A_1>0$) are attractive in nature and they compete each other to promote instability in the elastic and the viscous films, respectively. Figure 5 summarizes the LSA results for this case. In this discussion, we will find it useful to classify the elastic layer as *soft* when $G_2<10^6$ Pa and *hard* when $G_2>10^6$ Pa. In practice, polymer gels, biological membranes, etc., can be termed as soft elastic films because the typical shear moduli of these materials are in the range of kilopascals. Figures 5(a) and 5(b) show that, when h_{30} is kept constant and h_{10} is varied, free bilayers with soft (curve 1) and hard (curve 2) elastic films show similar ω_m vs H_r and λ_m vs H_r plots. The free bilayers with relatively thin viscous films (high H_r) are more unstable because of the strong destabilizing influence arising from Δg_1 that can easily deform the more compliant elastic film (high ω_m). Progressive increase in h_{10} (reduction in H_r) reduces the strength of the attractive force because of Δg_1 and, hence, the system shows a lesser degree of instability (low ω_m). The comparison between curves 1 and 2 shows that, at high H_r, when the elastic film is relatively thick, the bilayers with more compliant elastic films (low G_2 and high H_r) are more unstable (higher ω_m). It is interesting to note here that the increase in the strength of destabilizing intermolecular force because of Δg_1 by decreasing h_{10} leads to the reduction in λ_m [curves 1 and 2 in Fig. 5(b)] and this decay is much sharper when G_2 is small and h_{30} is high [curve 1 in Fig. 5(b)]. Therefore, as it was observed in the case of confined bilayers, λ_m of the free bilayers is a function of the intermolecular forces and material properties. Figures 5(c) and 5(d) show that, when the elastic film is soft and thin (low H_r), the strong intermolecular force because of Δg_3 imparts instability to the elastic layer (high ω_m in the curve 1) and the wavelengths of such instabilities are relatively small (low λ_m in the curve 1). The shear modulus (10^3 Pa) of the elastic film in the curve 1 indicates that polymer gels with thickness of ~10 nm can rapidly break up under the influence of strong intermolecular force because of Δg_3. With the increase in H_r, as the force because of Δg_3 becomes weaker, the system shows a smaller degree of instability (ω_m decreases). At some intermediate H_r, ω_m displays a minimum, where the force because of Δg_3 becomes weaker and the force because of Δg_1 becomes dominant to drive the instability. With further increase in H_r, the increased compliancy in the elastic layer increases instability in the bilayer (ω_m increases). In contrast to the bilayers with soft elastic films, the bilayers with hard elastic films [curve 2 in the Fig. 5(c)] are more stable (low ω_m) at low H_r because the increase in G_2 imparts extra stability to the elastic film. However, with progressive increase in H_r, the elastic layer becomes more compliant and the system shows a higher degree of instability (high ω_m). The curve 2 in the Fig. 5(d) shows that λ_m also progressively decay with the increase in H_r. However, at high H_r, a progressive increase in λ_m (decrease in ω_m) with h_{30} is observed. For bilayers with thick and hard elastic film (high H_r) at the top, the energy penalties for the deformations at the interfaces involving very short ($\lambda_m \ll h_{30}$) or very long ($\lambda_m \gg h_{30}$) wave are extremely large. Therefore, with increase in H_r, λ_m is always increased and adjusted to an intermediate wavelength domain (not too short or long) corresponding to the interfacial configuration for which the overall change in strain energy of the elastic film touches a minimum.[63]

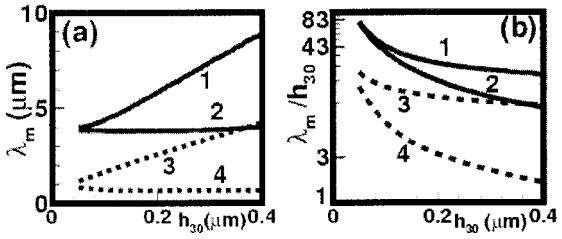

FIG. 6. LSA results for case 1 free bilayer. Plot (a) shows the variation of λ_m with h_{30} and plot (b) shows the variation of λ_m/h_{30} with h_{30}. Solid and broken lines in these plots correspond to $h_{10}=10$ and 5 nm, respectively. Curves 1 and 3 correspond to $G_2=10^7$ Pa and curves 2 and 4 correspond to $G_2=10^5$ Pa. In all the plots, $A_1=1.21\times10^{-20}$ J, $A_3=1.017\times10^{-20}$ J, and $\mu_1=1.0$ Pa s.

In Fig. 6, the sensitivity of λ_m on G_2 and h_{10} is shown. Figure 6(a) shows the variation of λ_m with h_{30} where the

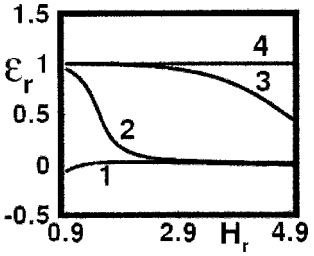

FIG. 7. LSA results for case 1 free bilayer. Variation of $\varepsilon_r=\varepsilon_2/\varepsilon_1$ with H_r when $h_{30}=20$ nm. Curves 1–4 correspond to 10^2, 10^3, 10^5, and 10^9 Pa shear moduli of the elastic layers, respectively. In all the plots, $A_3=3.58\times10^{-20}$ J, $A_2=1.05\times10^{-19}$ J, $A_1=4.47\times10^{-20}$ J, and $\mu_1=1.0$ Pa s.

solid and the broken lines are for different h_{10}. Curves 1 and 2 (or the curves 3 and 4) show that when the intermolecular force because of Δg_1 is constant, the bilayers with softer elastic films show a much shorter λ_m. In addition, curves 1 and 3 (or curves 2 and 4) show that when the elastic film is hard, a stronger intermolecular force because of Δg_1 leads to significant reduction of λ_m. In Fig. 6(b), we show the variation of λ_m/h_{30} with h_{30}. Curves 1 and 2 in Fig. 6(b) show that when the elastic films are hard and thin, $\lambda_m/h_{30}\sim80h_{30}$ and with increase in h_{30}, it decays to $\sim20h_{30}$. In contrast, curves 3 and 4 in Fig. 6(d) shows that bilayers with softer elastic films can lead to $\lambda_m/h_{30}\sim1$ when the elastic film thickness is >0.3 μm (curve 4). The results shown in Fig. 6 are interesting because it shows that the length scale of instability in the free bilayers can be reduced much below the film thickness by strengthening the destabilizing forces and reducing the elastic resistance, which opens up the possibility of further miniaturization of equilibrium patterns using these layered systems.

Figure 7 shows the variation of ε_r with H_r. In the free bilayers with soft elastic films (curve 1), the deformation at the elastic-viscous interface is always higher ($|\varepsilon_r|\ll1$) because the resistance from the capillary forces is smaller ($\gamma_{21}<\gamma_2$). At low H_r, the interfaces deform in squeezing mode ($\varepsilon_r<0$); otherwise, the bending mode prevails. Free bilayers with less compliant elastic films (curves 2 and 3) always deform in bending mode ($\varepsilon_r>0$). At high H_r, deformation at the elastic-viscous interface is high ($|\varepsilon_r|<1$), whereas at low H_r, as the compliancy of the elastic film reduces, almost equal deformations ($|\varepsilon_r|\sim1$) at the interfaces are observed. The bilayer with hard elastic films (curve 4) always deforms in bending mode ($\varepsilon_r>0$) with equal amplitude at the interfaces ($|\varepsilon_r|\sim1$). The results shown in Fig. 7 clearly infer that the free bilayers with less compliant elastic films are ideal candidates for transfer of patterns from the elastic-viscous interface to the elastic-air interface.

2. Case 2: Unstable elastic and stable viscous films ($A_1<0$ and $A_3>0$)

In this case, attractive intermolecular forces because of Δg_3 ($A_3>0$) promote instability in the elastic layer and the repulsive intermolecular forces because of Δg_1 imparts stability to the liquid film. Figure 8 summarizes the LSA results for this case. It essentially shows that the intermolecular forces because of Δg_3 can easily destabilize the soft polymer gels ($<10^4$ Pa) when the films are thin (<10 nm). Figure 8(a) shows that ω vs k plots in this case are bimodal in nature and with increase in h_{10} for a fixed h_{30}, the dominant mode of instability shifts from longer to shorter wavelength region. At small H_r, a thin elastic film is unstable under the influence of a strong attractive force because of Δg_3. Smaller capillary resistance at the elastic-viscous interface ($\gamma_2>\gamma_{21}$) causes the dominant mode of instability to stay there and λ_m remains shorter [curve 4 in Fig. 8(a) and broken lines in Fig. 8(b)]. With progressive reduction in increase in h_{10} (increasing H_r), the strength of the repulsive force arising from Δg_1 increases and the elastic-viscous interface becomes less deformable [ω_m decreases in Fig. 8(b)]. At high H_r, the strong stabilizing force arising from Δg_1 restricts the deformation of the elastic-viscous interface and, thus, the dominant mode of instability shifts to the elastic-air interface. Consequently, λ_m becomes larger [curve 1 in Fig. 8(a) and solid lines in Fig. 8(c)] because of the larger capillary resistance at the elastic-air interface ($\gamma_2>\gamma_{21}$). The shift of the dominant mode of instability at the interfaces exactly coincides with the

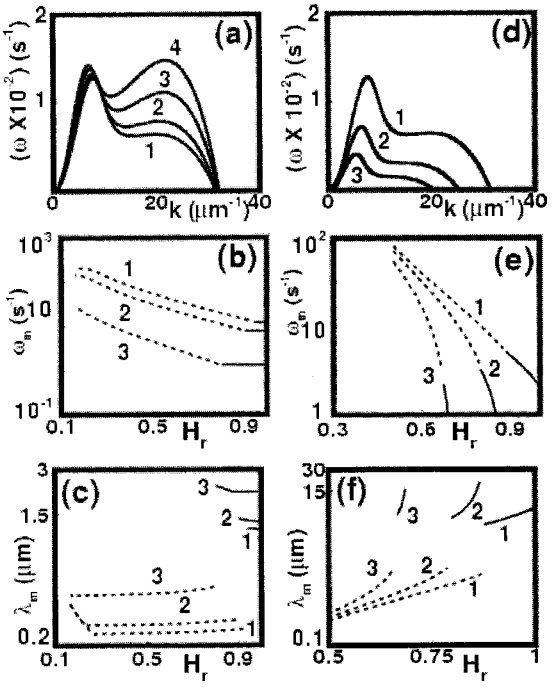

FIG. 8. LSA results for case 2 free bilayer. Plots (a) and (d) show the variation of ω with k. Curves 1–4 in plot (a) correspond to $h_{10}=5$, 5.5, 6.5, and 7.5 nm, respectively, when $h_{30}=5$ nm and $G_2=4\times10^3$ Pa. Plots (b) and (c) show the variations of ω_m and λ_m, respectively, with H_r when $h_{30}=5$ nm. Curves 1–3 correspond to $G_2=2\times10^3$, 4×10^3, and 8×10^3 Pa, respectively. Curves 1–3 in plot (d) correspond $h_{30}=5$, 5.5, and 6.0 nm, respectively, when $h_{10}=5$ nm and $G_2=4\times10^3$ Pa. Plots (e) and (f) show the variations of ω_m and λ_m, respectively, with H_r when $h_{10}=10$ nm. Curves 1–3 correspond to $G_2=10^3$, 2×10^3, and 4×10^3 Pa, respectively. The broken line and the solid line correspond to the short and long wavelength maxima, respectively. In all the plots, $A_3=3.3\times10^{-20}$ J, $A_2=-1.465\times10^{-20}$ J, $A_1=-4.29\times10^{-21}$ J, and $\mu_1=1.0$ Pa s.

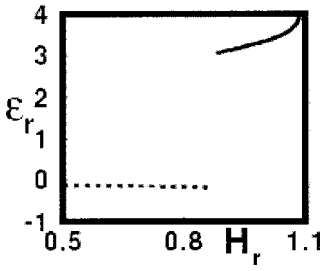

FIG. 9. LSA results for case 2 free bilayer. Variation of $\varepsilon_r=\varepsilon_2/\varepsilon_1$ with H_r when $h_{10}=10$ nm. In this plot, $A_3=3.3\times10^{-20}$ J, $A_2=1.465\times10^{-20}$ J, $A_1=-4.29\times10^{-2}$ J, $\mu_1=1.0$ Pa s, and $G_2=10^3$ Pa.

discontinuities in the broken and solid lines shown in Fig. 8(c) where λ_m jumps from a smaller to a larger value. Figures 8(d) and 8(e) show that with increase in h_{30} (increasing H_r), the destabilizing force because of Δg_3 becomes weaker and at high H_r, the strong restoring force in the elastic film completely stabilizes the system.

The switching of the dominant mode of instability from one interface to the other can be more distinctly shown through ε_r vs H_r in plot in Fig. 9. It shows that at low H_r, the elastic-viscous interface deforms more ($|\varepsilon_r|\ll1$) and the interfaces deform in squeezing mode ($\varepsilon_r<0$). However, at high H_r, $\varepsilon_r>1$ indicates that the instability evolves in bending mode and deformation is more at the elastic-air interface.

V. CONCLUSIONS

In addition to analyzing the length scale and dynamics of instabilities in bilayers composed of a soft elastic layer and a viscous layer, we show several strategies for the control and miniaturization of instability patterns in these bilayers. Two cases of bilayers are considered—a bilayer confined between two rigid surfaces and a free bilayer with two deformable interfaces. Given below is a summary of some physical insights regarding the pattern control based on the LSA pursued here.

The major conclusions for the confined bilayers can be summarized as follows. The instabilities in the confined bilayer can be initiated in two different ways: (A) A rigid contactor is increasingly brought closer to the elastic surface in a viscous medium until the onset of instability, which happens when the intersurface attraction overcomes the restoring elastic and surface tension forces. (B) A very thin solid polymer top coat is first applied to a soft elastomeric film, such that the bilayer configuration is highly unstable from the beginning, and then the amorphous polymer coat is melted to obtain the instability pattern. The previous theory[58,60–62] and experiments[63–65] of the elastic instability for a single layer show that the maximum pattern length scale, thus, obtained remains unchanged during the entire further cycle of greater adhesion and debonding because of this state being a local metaunstable state. However, further pattern miniaturization becomes possible by using an elastic-viscous bilayer because of two reasons: (A) The presence of an intercalated viscous film greatly reduces the strength of the stabilizing surface tension force because polymer-polymer interfacial tension is at least one order smaller than the surface tension. This aspect is especially effective in markedly reducing the length scale for the thinner (<0.5 μm) elastic films that are required for nanopatterning applications. (B) When the initial configuration of the bilayer prepared is such that the intersurface attractive force is much stronger than the stabilizing forces, the wavelength of the instability can be made shorter and precisely controlled by changing the viscous film thickness (intersurface interactions) and other material properties. The wavelength of instability in this configuration can be reduced by increasing the compliancy of the elastic film and strengthening the intersurface force. This not only opens up the possibilities of the miniaturization of structures using the confined bilayers but also the number of system variables to control the length scale of instability (e.g. film thicknesses, shear modulus of the elastic film, interfacial tension) are increased compared to the systems where the viscous film is absent.

The major conclusions obtained for the free bilayer are summarized below.

(a) The length and time scale of instability in the free bilayer is also a function of the intermolecular interaction and material properties. Therefore, by increasing the strength of the destabilizing intermolecular forces and reducing the elastic resistance of the elastic film, instabilities with shorter feature size can be achieved. This also opens up the possibility of miniaturization of instability patterns.

(b) Soft and thin elastic films, for example, polymer gels or biological membranes, floating on a viscous film and having a free bilayer configuration can rapidly break up under the influence of strong and destabilizing intermolecular force.

(c) Soft and thin elastic films at the top show the possibility of both squeezing and bending modes of instability with unequal deformation at the interfaces, whereas hard and thin elastic films at the top show only bending mode of instability with similar amplitude of deformations at the interfaces. Thus, free bilayers can be not only useful in the generation of patterns for a wide range of length scales including smaller feature size than that of the simpler systems studied, thus far, but also has the potential to transfer the pattern from the exposed surface to a buried interface.

ACKNOWLEDGMENTS

Discussions with Gaurav Tomar are gratefully acknowledged. This work was supported by the DST Unit on Nanosciences at IIT Kanpur.

APPENDIX: THE DISPERSION RELATIONS

The dispersion relation for the free bilayer,

$$\begin{vmatrix} 1 & -1 & 1/k & 1/k & 0 & 0 & 0 & 0 \\ 1 & 1 & 0 & 0 & 0 & 0 & 0 & 0 \\ J_1 & -J_2 & J_1J_5/k & -J_2J_6/k & -\omega J_1 & \omega J_2 & -\omega J_1J_5/k & \omega J_2J_6/k \\ J_1 & J_2 & h_1J_1 & h_1J_2 & -\omega J_1 & -\omega J_2 & -\omega h_1J_1 & -\omega h_1J_2 \\ k\mu_1J_1 & k\mu_1J_2 & \mu_1J_1J_5 & \mu_1J_2J_6 & -kG_2J_1 & -kG_2J_2 & -G_2J_1J_5 & -G_2J_2J_6 \\ 0 & 0 & 0 & 0 & kG_2J_3 & kG_2J_4 & G_2J_{11}J_3 & G_2J_{12}J_4 \\ -J_1J_{10}/\omega & J_2J_7/\omega & -h_1J_1J_{10}/\omega & h_1J_2J_7/\omega & J_{13} & J_{14} & J_{15} & J_{16} \\ J_1\phi_2/\omega & J_2\phi_2/\omega & h_1J_1\phi_2/\omega & h_1J_2\phi_2/\omega & J_3J_8 & J_4J_9 & h_2J_3J_8 & h_2J_4J_9 \end{vmatrix} = 0, \tag{A1}$$

where $J_1=e^{kh_1}$, $J_2=e^{-kh_1}$, $J_3=e^{kh_2}$, $J_4=e^{-kh_2}$, $J_5=(1+kh_1)$, $J_6=(-1+kh_1)$, $J_7=(2k\omega\mu_1+\phi_1)$, $J_8=(-2kG_2+\phi_4)$, $J_9=(2kG_2+\phi_4)$, $J_{10}=(2k\omega\mu_1-\phi_1)$, $J_{11}=(1+kh_2)$, $J_{12}=(-1+kh_2)$, $J_{13}=(2kG_2J_1+J_3\phi_2)$, $J_{14}=(-2kG_2J_2+J_4\phi_2)$, $J_{15}=(2kG_2h_1J_1+h_2J_3\phi_2)$, $J_{16}=-2kG_2h_1J_2+h_2J_4\phi_2$, $\phi_1=(-\gamma_{21}k^2+[\partial\pi_1/\partial h_1]-[\partial\pi_2/\partial h_1])$, $\phi_2=(\partial\pi_2/\partial h_1)$, and $\phi_4=(-\gamma_2k^2+[\partial\pi_2/\partial h_2])$. The dispersion relation for the confined bilayer,

$$\begin{vmatrix} 1 & -1 & 1/k & 1/k & 0 & 0 & 0 & 0 \\ 1 & 1 & 0 & 0 & 0 & 0 & 0 & 0 \\ J_1 & -J_2 & J_1J_5/k & -J_2J_6/k & -\omega J_1 & \omega J_2 & -\omega J_1J_5/k & \omega J_2J_6/k \\ J_1 & J_2 & h_1J_1 & h_1J_2 & -\omega J_1 & -\omega J_2 & -\omega h_1J_1 & -\omega h_1J_2 \\ k\mu_1J_1 & k\mu_1J_2 & \mu_1J_1J_5 & \mu_1J_2J_6 & -kG_2J_1 & -kG_2J_2 & -G_2J_1J_5 & -G_2J_2J_6 \\ 0 & 0 & 0 & 0 & kJ_3 & kJ_4 & J_{11}J_3 & -J_{12}J_4 \\ -J_1J_{10}/\omega & J_2J_7/\omega & -h_1J_1J_{10}/\omega & h_1J_2J_7/\omega & 2kG_2J_1 & -2kG_2J_2 & 2h_1kG_2J_1 & -2kG_2J_2h_1 \\ 0 & 0 & 0 & 0 & J_3 & J_4 & h_2J_3 & h_2J_4 \end{vmatrix} = 0, \tag{A2}$$

where $J_1=e^{kh_1}$, $J_2=e^{-kh_1}$, $J_3=e^{kh_2}$, $J_4=e^{-kh_2}$, $J_5=(1+kh_1)$, $J_6=(-1+kh_1)$, $J_7=(2k\omega\mu_1+\phi_1)$, $J_{10}=(2k\omega\mu_1-\phi_1)$, $J_{11}=(1+kh_2)$, $J_{12}=(-1+kh_2)$, and $\phi_1=(-\gamma_{21}k^2+[\partial\pi_1/\partial h_1])$.

[1] E. Ruckenstein and R. K. Jain, J. Chem. Soc., Faraday Trans. 2 **70**, 132 (1974).
[2] P. G. De Gennes, Rev. Mod. Phys. **57**, 827 (1985).
[3] F. Brochard-Wyart and J. Daillant, Can. J. Phys. **68**, 1084 (1990).
[4] F. Brochard-Wyart, P. Martin, and C. Redon, Langmuir **9**, 3682 (1993).
[5] A. Sharma, Langmuir **9**, 861 (1993).
[6] G. Reiter, R. Khanna, and A. Sharma, Phys. Rev. Lett. **85**, 1432 (2000).
[7] A. Sharma and A. T. Jameel, J. Colloid Interface Sci. **161**, 190 (1993).
[8] A. Oron, S. H. Davis, and S. G. Bankoff, Rev. Mod. Phys. **69**, 931 (1997).
[9] A. Sharma and R. Khanna, Phys. Rev. Lett. **81**, 3463 (1998).
[10] A. Sharma and R. Khanna, J. Chem. Phys. **110**, 4929 (1999).
[11] A. Oron, Phys. Rev. Lett. **85**, 2108 (2000).
[12] U. Thiele, M. Velarde, and K. Neuffer, Phys. Rev. Lett. **87**, 016104 (2001).
[13] D. Simmons and A. Chauhan, J. Colloid Interface Sci. **269**, 35 (2006).
[14] A. M. Higgins and R. A. L. Jones, Nature (London) **404**, 476 (2000).
[15] Z. Q. Lin, T. Kerle, S. M. Baker, D. A. Hoagland, E. Schaffer, U. Steiner, and T. P. Russell, J. Chem. Phys. **114**, 2377 (2001).
[16] Z. Q. Lin, T. Kerle, T. P. Russell, E. Schaffer, and U. Steiner, Macromolecules **35**, 3971 (2002).
[17] Z. Q. Lin, T. Kerle, T. P. Russell, E. Schaffer, and U. Steiner, Macromolecules **35**, 6255 (2002).
[18] P. Lambooy, K. C. Phelan, O. Haugg, and G. Krausch, Phys. Rev. Lett. **76**, 1110 (1996).
[19] Q. Pan, I. K. Winey, H. H. Hu, and R. J. Composto, Langmuir **13**, 1758 (1997).
[20] R. A. Segalman and P. F. Green, Macromolecules **32**, 801 (1999).
[21] M. D. Morariu, N. E. Voicu, E. Schaffer, Z. Lin, T. P. Russel, and U. Steiner, Nat. Mater. **2**, 48 (2003).
[22] N. Bowden, S. Brittain, A. G. Evans, J. W. Hutchinson, and G. M. Whitesides, Nature (London) **393**, 146 (1998).
[23] P. J. Yoo, S. Y. Park, K. Y. Suh, and H. H. Lee, Adv. Mater. (Weinheim, Ger.) **14**, 1383 (2002).
[24] P. J. Yoo and H. H. Lee, Phys. Rev. Lett. **91**, 154502 (2003).
[25] P. J. Yoo, K. Y. Suh, H. Kang, and H. H. Lee, Phys. Rev. Lett. **93**, 034301 (2004).
[26] P. J. Yoo and H. H. Lee, Macromolecules **38**, 2820 (2005).
[27] S. J. Kwon, J. G. Park, and S. H. Lee, J. Chem. Phys. **122**, 031101 (2005).
[28] E. R. de Souza and D. Gallez, Phys. Fluids **10**, 1804 (1998).
[29] W. T. Coakley, D. Gallez, E. R. de Souza, and H. Gauci, Biophys. J. **77**, 817 (1990).
[30] R. K. Jain and E. Ruckenstein, J. Colloid Interface Sci. **54**, 108 (1976).
[31] C. H. Maldarelli, R. K. Jain, I. B. Ivanov, and E. Ruckenstein, J. Colloid Interface Sci. **78**, 118 (1980).
[32] K. D. Danov, V. N. Paunov, N. Alleborn, H. Raszillier, and F. Durst, Chem. Eng. Sci. **53**, 2809 (1998).
[33] K. D. Danov, V. N. Paunov, S. D. Stoyanov, N. Alleborn, H. Raszillier, and F. Durst, Chem. Eng. Sci. **53**, 2823 (1998).
[34] V. N. Paunov, K. D. Danov, N. Alleborn, H. Raszillier, and F. Durst, Chem. Eng. Sci. **53**, 2839 (1998).
[35] A. Pototsky, M. Bestehorn, D. Merkt, and U. Thiele, Phys. Rev. E **70**, 025201 (2004).
[36] D. Bandyopadhyay, R. Gulabani, and A. Sharma, Ind. Eng. Chem. Res. **44**, 1259 (2005).
[37] L. S. Fisher and A. A. Golovin, J. Colloid Interface Sci. **291**, 515 (2005).
[38] A. Pototsky, M. Bestehorn, D. Merkt, and U. Thiele, J. Chem. Phys. **122**, 224711 (2005).
[39] D. Bandyopadhyay and A. Sharma, J. Chem. Phys. **125**, 054711 (2006).
[40] A. Pototsky, M. Bestehorn, D. Merkt, and U. Thiele, Europhys. Lett. **74**, 665 (2006).
[41] D. Merkt, A. Pototsky, M. Bestehorn, and U. Thiele, Phys. Fluids **17**, 064104 (2005).
[42] Z. Suo, J. Mech. Phys. Solids **43**, 829 (1995).
[43] W. T. S. Huck, N. Bowden, P. Onck, T. Pardoen, J. W. Hutchinson, and G. M. Whitesides, Langmuir **16**, 3497 (2000).
[44] N. Sridhar, D. J. Srolovitz, and Z. Suo, Appl. Phys. Lett. **78**, 2482 (2001).
[45] N. Sridhar, D. J. Srolovitz, and B. N. Cox, Acta Mater. **50**, 2547 (2002).
[46] E. Cerda and L. Mahadevan, Phys. Rev. Lett. **90**, 074302 (2003).
[47] X. Chen and J. W. Hutchinson, J. Appl. Mech. **71**, 597 (2004).
[48] R. Huang and Z. Suo, J. Appl. Phys. **91**, 1135 (2002).
[49] R. Huang, J. Mech. Phys. Solids **53**, 63 (2005).

[50] S. H. Im and R. Huang, J. Appl. Mech. **72**, 955 (2005).
[51] Z. Y. Huang, W. Hong, and Z. Suo, J. Mech. Phys. Solids **53**, 2101 (2005).
[52] A. Martin, O. Rossier, A. Buguin, P. Auroy, and F. Brochard-Wyart, Eur. Phys. J. E **74**, 665 (2000).
[53] A. E. Hosoi and L. Mahadevan, Phys. Rev. Lett. **93**, 137802 (2004).
[54] S. Kumar and O. K. Matar, J. Colloid Interface Sci. **273**, 581 (2004).
[55] O. K. Matar, V. Gkanis, and S. Kumar, J. Colloid Interface Sci. **286**, 319 (2005).
[56] A. Ghatak, M. K. Chaudhury, V. Shenoy, and A. Sharma, Phys. Rev. Lett. **85**, 4329 (2000).
[57] W. Monch and S. Herminghaus, Europhys. Lett. **53**, 525 (2001).
[58] V. Shenoy and A. Sharma, Phys. Rev. Lett. **86**, 119 (2001).
[59] C. Q. Ru, J. Appl. Phys. **90**, 6098 (2001).
[60] V. Shenoy and A. Sharma, Langmuir **18**, 2216 (2002).
[61] J. Sarkar, V. Shenoy, and A. Sharma, Phys. Rev. Lett. **93**, 018302 (2004).
[62] J. Sarkar, A. Sharma, and V. Shenoy, Langmuir **21**, 1457 (2005).
[63] M. Gonuguntla, A. Sharma, R. Mukherjee, and S. A. Subramanian, Langmuir **22**, 7066 (2006).
[64] M. Gonuguntla, A. Sharma, J. Sarkar, S. A. Subramanian, M. Ghosh, and V. Shenoy, Phys. Rev. Lett. **97**, 018303 (2006).
[65] M. Gonuguntla, A. Sharma, and S. A. Subramanian, Macromolecules **39**, 3365 (2006).
[66] S.-Q. Huang, Q.-Y. Li, X.-Q. Feng, and S.-W. Yu, Mech. Mater. **38**, 88 (2006).
[67] L. D. Landau and E. M. Lifshitz, *Theory of Elasticity* (Pergamon, London, 1959).
[68] J. N. Israelachvili, *Intermolecular and Surface Forces* (Academic, London, 1992).
[69] C. J. van Oss, M. K. Chaudhury, and R. J. Good, Chem. Rev. (Washington, D.C.) **88**, 927 (1988).